PCCP

ROYAL SOCIETY OF CHEMISTRY

PAPER

Published on 22 June 2026

Cite this: DOI: 10.1039/d6cp00917d

Bridging calculated charges and formal oxidation state of manganese oxides: a DFT/DFT+*U* study

Julie-Ann Hoffman, [a] Enrico Sireci,[b] Thobani Gambu, [a] Dmitry I. Sharapa, [b] Felix Studt [bc] and Eric van Steen *[a]

Received 12th March 2026,
Accepted 22nd June 2026

DOI: 10.1039/d6cp00917d

rsc.li/pccp

Bridging the gap between theoretically predicted and measured metal oxides charges is crucial when using synergistically computational and experimental techniques to ensure reliability of the models. Manganese oxide, with its wide range of oxidation states, is an ideal candidate for probing this relationship. Here, we conducted a magnetic moment and Bader charge analysis using two different exchange correlation functionals, *i.e.* RPBE and BEEF-vdW, both with DFT (U = 0 eV) and DFT+U (U = 2.5 eV), on several bulk and cluster manganese oxides with formal Mn oxidation states ranging between +1 and +7. We found that the relationship between Mn formal oxidation states and magnetic moments in both bulk and molecular structures can be described accurately by a quadratic fit. In comparison, the relationship between formal oxidation states and Bader charge is more uncertain, and could be fit by a single hyperbolic function only upon correction of the formal oxidation state *via* the Madelung constant. Finally, we employed the derived correlations to predict the formal oxidation state of Mn in different $Mn_xO_yH_z$ clusters on fcc-Co(111). Both methods predict that the Mn oxidation states largely do not align with the stoichiometry of the clusters. While the magnetic moments correlation always yielded Mn oxidation states of +2, the results obtained from the Bader charges were more dependent on the cluster stoichiometry.

Introduction

The concept of formal oxidation state assigned to ions in a structure is central to our understanding on the structure and chemistry of materials.[1] However, metal atoms in ionic structures are more accurately describe by partial charges, arising from a partial covalency (and partial ionicity) of the bonds. Nevertheless, the ionic model remains prevalent in describing transition metal oxides,[2] which may lead to an incorrect prediction and understanding of their properties. For instance, Yang *et al.*[3] calculated the Bader charge for Ce in CeO_2 and Ce_2O_3 on Cu(111) surface; these were found to be +2.27*e* and +2.02*e*, respectively. This is much lower than their formal oxidation state of +4 and +3. Due to this mismatch, the authors extrapolated the value of Ce in the cluster to obtain a formal oxidation state of +2.93*e*. This alludes to a disconnect between the understanding of the electronic charge present within a bulk crystalline structure compared to clusters which are studied on surfaces. The relation between formal and physical oxidation state has been extensively researched in the field of molecular transition metals over decades to connect theoretical predictions and experimental measurements.[4–14] The physical oxidation state is defined measured electron density localised on an atom which can be evaluated by both spin density and charge density distributions using computational chemistry quantum mechanical methods.[15]

Here, we attempt to resolve the relationship between these charge definitions by investigating both spin and charge density for manganese in manganese oxide bulk structures and clusters as well as manganese oxides clusters deposited on a metal.

Manganese oxides are a unique class of compounds due to their wide range of oxidation states (commonly +2, +3, +4, ranging up to +7) and complex magnetic behaviours. Owing to this, these materials have a variety of potential applications in electrode materials for batteries[16–18] as magnetic materials for transformer cores[19–22] and in catalysis.[23] In the latter field, one of the applications of Mn oxide is promotion of cobalt-based Fischer–Tropsch catalysts to boost their activity and C_{5+} selectivity, where it is expected to be present as oxidic clusters on the catalytically active cobalt metal surface.[24–29] More generally, transition metal (TM) oxide clusters on metal surfaces, such as CeO_x on Cu[3], Au[30] and Ag,[31] TiO_x on Pt[32] and FeO_x on Pt,[33] are widely discussed systems in catalytic applications, and in particular when the focus is on so-called "inverse" catalysts, that are usually studied to better understand the electronic metal–support interactions.[34]

[a] *Catalysis Institute, Department of Chemical Engineering, University of Cape Town (UCT), P.O. Box X3, Rondebosch 7701, Cape Town, South Africa. E-mail: eric.vansteen@uct.ac.za*
[b] *Institute of Catalysis Research and Technology (IKFT), Karlsruhe Institute of Technology (KIT), 76344 Eggenstein-Leopoldshafen, Germany*
[c] *Institute for Chemical Technology and Polymer Chemistry, Karlsruhe Institute of Technology, 76131 Karlsruhe, Germany*

When investigating these systems, DFT calculations are routinely used in combination with experimental techniques to elucidate the role of the TM oxides structures. In this regard, experiments often measure TM oxidation states, that can in principle be used to rationally guide the definition of the computational models. Nevertheless, the correlation between measured oxidation state and actual cluster stoichiometry is complicated by the presence of the metal surface that acts as a reservoir of electrons, which may compensate for the charge transfer from the TM centres to the binding oxygen anions.

Different methods have been developed within the DFT formalism to infer atomic charges from the electron density (ρ),[35] of which probably the most popular is the Bader model.[36–38] In this framework, (Bader) volumes are defined around the atoms considering electron density zero-flux surfaces ($\nabla\rho(\mathbf{r})\cdot\mathbf{n}(\mathbf{r}) = 0$) as spatial boundaries, and the electron density is consequently integrated over these volumes to assign partial atomic charges. A fundamentally different approach is to rely on the atomic magnetic moments to resolve TM ions valence, that are obtained by integrating the difference between the spin-up and spin-down electron densities within a certain portion of volume, that can either be a sphere centred on the atom with a radius defined by the user, or the atomic orbitals (defined according to the employed basis set) onto which the electron density is projected.[39–42] Nonetheless, both the Bader charges and the atomic magnetic moments cannot be used directly to derive the formal oxidation state, which is the quantity that experimentalists using techniques such as X-ray absorption spectroscopy (XAS) and X-ray photoelectron spectroscopy (XPS) refer to.

In this work, the relations between the formal oxidation state of manganese oxides and calculated Bader charges and atomic magnetic moment on the Mn centre were investigated using the RPBE and BEEF-vdW XC functionals, both with DFT and DFT+U. Manganese oxide bulk and gas-phase molecular structures with known formal oxidation states were evaluated, from which we derived correlations to describe changes in the formal Mn valence with Bader charges and atomic magnetic moments. Finally, we employ the derived correlations to predict the oxidation state of several $Mn_xO_yH_z$ clusters on fcc-Co(111) as a case study. Our results show that while the dependency of the formal oxidation state on the atomic magnetic moments is rather well-defined for both cluster and bulk Mn oxide structures, that on the Bader charges is more uncertain. We found that the two approaches can yield moderately different quantitative results, but both predict that charge transfer from the Co surface prevents Mn from assuming an oxidation state $\geq$+3. Overall, this study presents a method for correlating theoretical calculations and experimental observations, and it is postulated that it may be useful for understanding the electronic charge present in other systems.

Computational details

DFT calculations

Spin-polarized quantum chemical calculations were performed using the Vienna *Ab Initio* Simulation Package (VASP) code.[43,44] The generalized gradient approximation (GGA) exchange correlation (XC) functionals RPBE[45] and BEEF-vdW[46] were used with the projector augmented wave (PAW) method.[47,48] Plane wave basis set with kinetic energy cut-off of 600 eV and 400 eV were used for the bulk crystalline structures and the clusters of manganese oxides, respectively. The Brillouin zone was sampled using a Monkhorst–Pack k-point grid[49] of $8 \times 8 \times 12$ for bulk MnO_2, $6 \times 6 \times 4$ for bulk Mn_3O_4, $4 \times 4 \times 4$ for bulk MnO and bulk Mn_2O_3 and a k-point grid of $1 \times 1 \times 1$ for all gas-phase clusters. Additionally, a k-point grid density of $\sim$36 k-points per $Å^{-1}$ was employed for all $Mn_xO_yH_z$ clusters on fcc-Co(111). The convergence threshold for the self-consistent field cycles was set at 10^{-6} eV and a Gaussian smearing with a width of 0.1 eV was applied for all studied structures. Ionic convergence was achieved when the maximum force acting on the atoms was below 0.01 eV $Å^{-1}$. Four layers fcc-Co(111) slabs were employed, of which the bottom two layers were frozen in their bulk configuration, while the upper two layers were allowed to relax. At least 20 Å of vacuum was included in the slab models. Bader charge analysis[36–38,50] was performed on the optimized structures of the bulk crystalline and clusters of manganese oxides in order to evaluate the electronic charge present on manganese.

DFT methods have the tendency to underestimate electronic properties, particularly for metal oxides.[51] In this study, the use of a single calibrated value for the Hubbard (U) correction or DFT+U method[52] with U_{eff} = 2.5 eV was investigated as an approach to compensate this underestimation. This was the optimal value found upon U_{eff} calibration by matching the calculated and experimental ΔH^0_{rxn} of oxidation of MnO to Mn_3O_4, Mn_2O_3 and MnO_2.[35,37] However, it must be noted that for complex systems such as manganese oxides that exhibit multiple spin configurations and varying oxidation states, that the fitting accuracy of a U parameter is not straightforward.[53,54] (see U_{eff} calibration given in Section S1 in the SI, for more detailed explanation). Furthermore, to reveal any systematic errors that may occur while employing a single U value across all the systems, DFT calculations of all computational models used for deriving the oxidation state correlations were carried out both with and without the Hubbard correction.

$$3MnO + H_2O \rightarrow Mn_3O_4 + H_2 \quad (1)$$

$$2MnO + H_2O \rightarrow Mn_2O_3 + H_2 \quad (2)$$

$$MnO + H_2O \rightarrow MnO_2 + H_2 \quad (3)$$

The ΔH^0_{rxn} for reactions (1)–(3) were calculated using

$$\Delta H^0_{rxn} = \Delta H^0_f(Mn_xO_{(x+1)}) + \Delta H^0_f(H_2) - x\Delta H^0_f(MnO) \quad -\Delta H^0_f\ (H_2O) \quad (4)$$

using H_2O and H_2 as the oxidation couple to avoid including O_2 in the calculations, whose bond energy is overestimated by GGA functionals.[45,55,56] We have included the ZPE and enthalpy change contributions both for the gas-phase molecules and investigated solids. Further details about the calculation of the phonons in the investigated bulk structures are given in Section S1 in the SI.

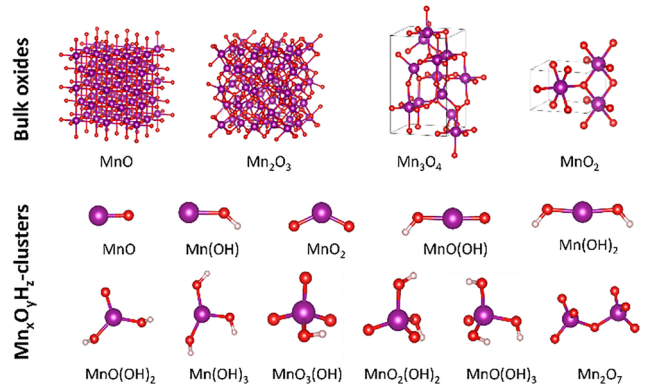

Fig. 1 Bulk crystalline structures of manganese oxides with Mn oxidation state ranging from +2 to +4, and clusters of manganese oxide and manganese hydroxides with Mn oxidation state ranging from +1 to +7, visualized using VESTA[61] (Mn: purple; O: red; H: white).

Computational models

Fig. 1 displays the models of the various bulk structures and clusters of manganese oxides that were studied. Manganese(II)oxide,[57] MnO assumes a rock salt structure (space group $Fm\bar{3}m$, #225) with Mn^{2+} and O^{2-} present in 6 : 6 octahedral coordination and modelled with an antiferromagnetic (AFM) ordering along the (111) planes. Manganese(III)oxide,[58] α-Mn_2O_3, a cubic bixbyite structure (space group $Ia\bar{3}$, #206), was modelled as a tetragonal phase, with O^{2-} coordinated to Mn^{3+} in a dislocated octahedral position with the Mn ions present in a ferromagnetic (FM) arrangement. Manganese(II,II)oxide,[59] Mn_3O_4, known as hausmannite, was modelled as spinel structure (space group $I4_1/amd$, #141), with Mn^{2+} occupying the tetrahedral sites and Mn^{3+} occupying the octahedral sites within the crystal where the Mn ions are present in FM ordering. Manganese(IV)oxide,[60] β-MnO_2, is modelled as a tetragonal lattice (space group $P4_2/mnm$, #136). The octahedral configuration of Mn^{4+} and O^{2-} are modelled with AFM magnetic ordering. Several manganese oxides and manganese hydroxide clusters were investigated in this study with an assigned oxidation state ranging from +1 to +7. These clusters were modelled in asymmetrical unit cells with dimensions of 12 Å × 13 Å × 14 Å (see Table S4).

Results and discussion

Geometric and magnetic structure

The geometry and magnetic properties of the optimised bulk Mn oxides structures and clusters were assessed by examining the lattice constants of the bulk Mn oxides, the bond lengths of the Mn oxide clusters and the spin orientations in the bulk Mn oxides, as well as magnetic moments for all structures. Table S3 shows the calculated crystal lattice parameters for DFT (U = 0 eV) and DFT+U (U = 2.5 eV) for both RPBE and BEEF-vdW XC functionals, and experimental lattice constants for the crystalline structures sourced from literature.[57,62–64] The calculated crystal lattice constants for all the bulk MnO, Mn_3O_4, Mn_2O_3 and MnO_2 structures were found to be in good agreement with the experimental values, where the relative percent error was between 0.9–3.0%. In particular, the lattice constants calculated with the DFT+U method, were smaller relative values obtained with plain DFT. Whilst comparison across the different XC functionals showed that bulk Mn oxides calculated with RPBE were larger relative to the BEEF-vdW XC functional. The bond lengths for the Mn oxide clusters were found to be within the typical range reported in literature for Mn–O bond lengths 1.61–1.83 Å[65,66] (see Table S5 for both the RPBE and BEEF-vdW XC functionals, respectively). Notably, unlike the trend seen for lattice constants in the bulk Mn oxide structures, the bond lengths calculated with DFT+U (U = 2.5 eV) were slightly larger compared to those calculated without the Hubbard correction. This elongation in bond length has been reported in literature and is postulated to occur due to increased electron localization narrowly distributed over the small clusters, even though it is dependent on the system studied.[67]

Due to the varying oxidation states, Mn oxides exhibit complex magnetic behaviour as well as different spin orientations.[7] In this study, the bulk Mn oxides were calculated with AFM ordering for MnO and MnO_2, while Mn_3O_4 and Mn_2O_3 had FM ordering. This is evident in Table S6, from the signs (+/−) associated with the up/down spin orientation of the magnetic moments for each Mn in the bulk Mn oxides. The magnetic moments (μ_B) of both the bulk and cluster Mn oxide structures were investigated (see Table 1 and Table 2 for the RPBE XC functional). Both XC functionals had similar magnetic moments, for each DFT (U = 0 eV) or DFT+U (U = 2.5 eV) approach taken, where the standard

Table 1 Calculated magnetic moment using RPBE XC functional on Mn in bulk crystalline manganese oxide

Formal oxidation state on Mn		Average magnetic moment on Mn[a] (μ_B)	
		DFT (U = 0 eV)	DFT+U (U = 2.5 eV)
MnO	+2	4.36	4.54
Mn_3O_4	+2/+3	3.98	4.14
Mn_2O_3	+3	3.76	3.96
MnO_2	+4	2.60	2.94

[a] Magnetic moments are reported as absolute values.

Table 2 Calculated magnetic moment using RPBE XC functional on Mn in $Mn_xO_yH_z$ clusters

	Formal oxidation state on Mn	Average magnetic moment on Mn[a] (μ_B)	
		DFT (U = 0 eV)	DFT+U (U = 2.5 eV)
MnOH	+1	4.66	4.79
MnO	+2	3.91	4.19
$Mn(OH)_2$	+2	4.28	4.46
MnO(OH)	+3	3.67	4.10
$Mn(OH)_3$	+3	3.56	3.80
MnO_2	+4	2.68	3.17
$MnO(OH)_2$	+4	2.70	3.02
$MnO(OH)_3$	+5	1.76	2.07
$MnO_2(OH)_2$	+6	0.92	1.18
Mn_2O_7	+7	0.00	0.00
$MnO_3(OH)$	+7	0.00	0.00

[a] Magnetic moments are reported as absolute values.

deviation between the RPBE and BEEF-vdW XC functionals, were $\pm 0.01\mu_B$ and $\pm 0.02\mu_B$, for DFT and DFT+U, respectively (see Table S7). The Hubbard correction had a bigger effect since the magnetic moments calculated with optimal U_{eff} = 2.5 eV were notably higher than those calculated with U = 0 eV and closer to experimental values, thus showing that DFT+U improves the description of the magnetic moments.

The Mn oxide clusters showed similar atomic magnetic moments to their bulk Mn oxide counterparts, in particularly for the DFT+U (U = 2.5 eV) approach. MnO and $Mn(OH)_2$ clusters have an atomic magnetic moment of $\sim 4.2\mu_B$ and $4.5\mu_B$, which is similar to that of bulk MnO that has a magnetic moment of $\sim 4.6\mu_B$. The high atomic magnetic moment is consistent with the high spin $3d^5$ configuration of Mn^{2+}. A similar high magnetic moment was seen for MnO(OH) ($4.2\mu_B$) and $Mn(OH)_3$ ($3.8\mu_B$) clusters, which is comparable to the atomic magnetic moment of bulk Mn_2O_3 of $\sim 4.0\mu_B$, in line with the high spin $3d^4$ configuration of Mn^{3+}. Lastly, the MnO_2 and $MnO(OH)_2$ clusters had magnetic moments of $\sim 2.9\mu_B$ and $3.0\mu_B$, respectively corresponding well with the atomic magnetic moment $\sim 2.9\mu_B$ of bulk MnO_2 and the high spin $3d^3$ configuration of Mn^{4+}.

Fig. 2 displays the relationship between the assigned formal oxidation state on Mn for the bulk and clusters of Mn oxide and their magnetic moments for the RPBE XC functional (See Fig. S3 for the corresponding data for the BEEF-vdW XC functional). It is shown that the atomic magnetic moments *vs.* formal oxidation state correlations are remarkably well described by a quadratic fit, with R^2 values of 0.99 for RPBE, RPBE + U, BEEF-vdW and BEEF-vdW+U. This gradual decrease in magnetic moment, displayed by the quadratic fit, with increasing formal oxidation state is consistent with strong metal–ligand covalency.[68] Furthermore, this progressive Mn 3d orbital depopulation is exhibited by the decrease in the pDOS peaks of gas-phase molecular structures, with increasing assigned formal oxidation state (see Fig. S4). Interestingly, for oxidation state ≥ 3, we report a near 1 : 1 correspondence between the increase in formal oxidation state and the decrease of the atomic magnetic moment reflecting the progressive depopulation of the Mn 3d orbitals and reveals that it is possible to almost directly infer the Mn valence from its magnetic moment. Importantly, we show that a single relation is suitable to describe simultaneously both bulk and gas-phase molecular structures, suggesting that this approach can be successfully applied to systems that are qualitatively very different. To access the reliability of the data correlation seen, the VASP on-site-partial charge densities[69] of Mn for the RPBE XC functional (U = 0) were compared to the atomic magnetic moment values. This charge population analysis method uses same charge partitioning that is utilised for the magnetic moment, which is based on the integration of projection of localised orbitals onto atomic spheres defined by the PAW method, which are decomposed into their local quantum numbers (l·m).[69] The linear correlation between the on-site partial charge densities and atomic magnetic moments was found to be in fair agreement with R^2 value of 0.89 in the parity plot (see Fig. S5). Additionally, the DDEC6 atomic population analysis[70] was performed to ensure that the results shown were not dependent on approach used. This method is the revision of density derived electrostatic and chemical (DDEC) approach, where the charge and spin partitioning are based on atom-centered integration grids, and includes core electron density correction.[70,71] Here, the trend seen for the atomic magnetic moments was evaluated against the atomic spin moments (ASMs) derived from DDEC6 atomic population analysis (the spin moments are in fair agreement with each other with a R^2 value of 0.91 in the parity plot; see Fig. S6).

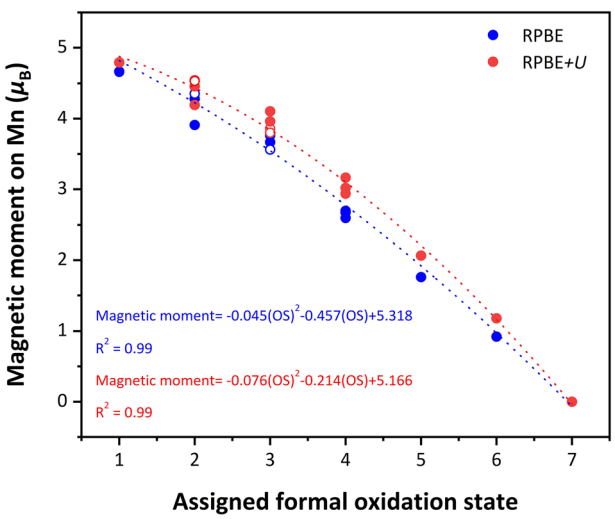

Fig. 2 Assigned formal oxidation state on Mn for the manganese oxides studied *vs.* their magnetic moments for both DFT (U = 0 eV) and DFT+U (U = 2.5 eV) method for the RPBE XC functional (open symbols: bulk manganese oxide; solid symbols: $Mn_xO_yH_z$ clusters; OS: oxidation state).

Bader charge analysis

Table 3 shows the obtained averaged Bader charge per manganese atom in the various bulk Mn oxide structures of assigned formal oxidation state for manganese, for RPBE XC functional calculated using DFT (U = 0 eV) and DFT+U (U = 2.5 eV), respectively (see Table S8 for corresponding data for BEEF-vdW XC functional). For the Bader charge calculations, it is evident that an increase in assigned formal oxidation state of manganese corresponds to an increase in the Bader charge calculated with both XC functionals and for both the DFT and DFT+U method. The two functionals yield nearly the same Bader charge values for Mn with differences $\leq 2\%$. The DFT+U

Table 3 Calculated net Bader charge using RPBE XC functional on Mn for bulk crystalline manganese oxides

	Formal oxidation state on Mn	Bader charge on Mn (e)	
		DFT (U = 0 eV)	DFT+U (U = 2.5 eV)
MnO	+2	+1.334	+1.357
Mn_3O_4	+2	+1.456	+1.461
Mn_3O_4	+3	+1.602	+1.645
Mn_2O_3	+3	+1.636	+1.663
MnO_2	+4	+1.770	+1.824

calculations of the bulk Mn oxides, excluding charge for the bulk Mn_2O_3 for the RPBE XC functional, resulted in higher Bader charge than the Bader charge on manganese in the clusters. As the DFT+U method has an additional on-site potential of 2.5 eV on each manganese atom, it is expected that Bader charge values would be higher than obtained with DFT(U = 0 eV). This may be negated by the elongation in the lattice parameters (see Table 3 and Table S3) in the optimised bulk Mn oxides when using the Hubbard correction.

Table 4 displays the average Bader charge per manganese atom in the manganese oxides and manganese hydroxides clusters that were investigated for the RPBE XC functional, calculated using DFT (U = 0 eV) and DFT+U (U = 2.5 eV) (see Table S9 for the corresponding data for the BEEF-vdW XC functional). Similarly, to the trends seen for the bulk crystalline structures, as the assigned formal oxidation state increases, the Bader charge for DFT and DFT+U method increases as well. Additionally, as seen in the bulk Mn oxides, the different XC functionals result in similar Bader charge values for manganese in Mn oxide clusters with an average difference $\lesssim$2%. Furthermore, the Bader charge for manganese in $Mn_xO_yH_z$ clusters was on average $\lesssim$5% higher, when calculated using the DFT+U method compared to the Bader charge calculated using the DFT (U = 0 eV) method. Notably, given the formal oxidation state, the nature of the ligands binding to Mn can significantly affect the calculated Bader charge. For example, for the RPBE XC functional we observe a difference in the Bader charge on manganese in MnO and $Mn(OH)_2$ of 0.377e and 0.446e for DFT (U = 0 eV) and DFT+U (U = 2.5 eV) method, respectively, although the same formal oxidation state is identical in both systems. Interestingly, we observe that the Bader charge *vs.* oxidation state relation is somewhat inconsistent for bulk Mn oxides as well with Mn^{2+} ions in bulk MnO and Mn_3O_4 displaying a notable Bader charge difference of 0.122e and 0.104e for the DFT (U = 0 eV) and DFT+U (U = 2.5 eV) method, respectively.

Fig. 3 displays the Bader charge on manganese in bulk manganese oxides and in $Mn_xO_yH_z$ clusters as a function of its formal oxidation state, for both DFT (U = 0 eV) and DFT+U (U = 2.5 eV) methods using the RPBE XC functional (see Fig. S7 for the BEEF-vdW XC functional) to evaluate the relationship between the Bader charge of the bulk structures and clusters of Mn oxides studied. For this brief analysis, only data points with a formal oxidation state up to and including +4 were considered. Overall, the linear fit between the Bader charge and the formal oxidation state is poor, with a R^2 value is 0.55 for both the DFT (U = 0 eV) and DFT+U (U = 2.5 eV) method. Thus, indicating that this current model is not robust. Nevertheless, the p-value for the slopes was 0.00564 and 0.00561, respectively, which is significantly lower than significance level of 0.05 implying a correlation between the Bader charge and the formal oxidation state. In addition, the trend seen for the Bader charge on Mn for the RPBE was also evaluated against the net atomic charges (NACs) derived from DDEC6 atomic population analysis.[70] Here, similarly to the magnetic moments, the Bader charge and the NAC were found to be in fair agreement with each other with a R^2 value of 0.90 in the parity plot(see Fig. S9). Furthermore, it can be observed that the Bader charge on manganese for bulk manganese oxides were positioned above the line-of-best-fit, whilst the Bader charge of manganese in the clusters were mainly positioned below the line-of-best-fit. It is thus apparent that Bader charge-formal charge relationship for manganese in bulk manganese oxide and in $Mn_xO_yH_z$ clusters and bulk Mn oxide structures are not identical.

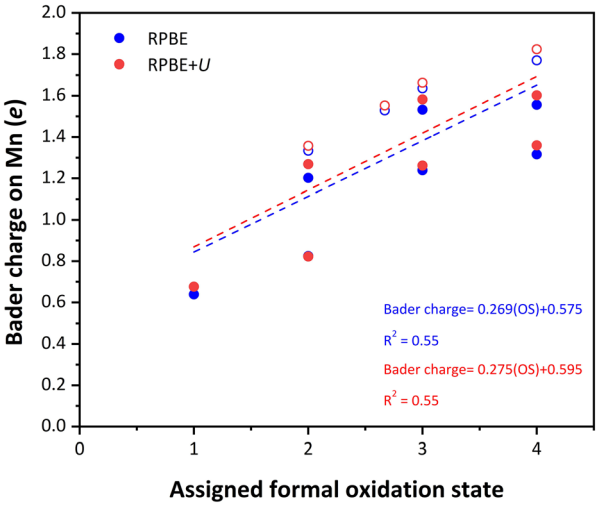

Fig. 3 Bader charge present on Mn *vs.* their assigned formal oxidation state for both DFT (U = 0 eV) and DFT+U (U = 2.5 eV) method for the RPBE XC functional (open markers: bulk manganese oxide; solid markers: $Mn_xO_yH_z$ clusters; OS: oxidation state).

Table 4 Calculated Bader charge using RPBE XC-functional on Mn in $Mn_xO_yH_z$ clusters

	Formal oxidation state on Mn	Bader charge on Mn (e)	
		DFT (U = 0 eV)	DFT+U (U = 2.5 eV)
MnOH	+1	+0.639	+0.677
MnO	+2	+0.825	+0.822
$Mn(OH)_2$	+2	+1.202	+1.268
MnO(OH)	+3	+1.239	+1.262
$Mn(OH)_3$	+3	+1.533	+1.582
MnO_2	+4	+1.316	+1.359
$MnO(OH)_2$	+4	+1.556	+1.602
$MnO(OH)_3$	+5	+1.711	+1.737
$MnO_2(OH)_2$	+6	+1.711	+1.566
Mn_2O_7	+7	+1.771	+1.719
$MnO_3(OH)$	+7	+1.773	+1.640

The Bader charge originates from the spatial distribution of the electron density, which in periodic systems is not only affected by the presence of adjacent ions, but also by the long-range coulombic interactions typically captured by the structure-dependent Madelung constant, a dimensionless quantity to account for the total coulombic interactions of the ions in a crystal structure.[72,73] As such the incorporation of the Madelung constant should result in a better description of the electrostatic contributions to the electron density. Henceforth, it can be argued that the Bader charge on manganese in a periodic, ionic

structure is not only affected by the formal oxidation state of manganese, but rather by the electro-static contribution induced by manganese given by an effective charge, *i.e.*, the formal oxidation state of manganese in an ionic structure attenuated by the Madelung constant. A crude approximation approach was initially employed to determine the Madelung constants for the bulk manganese oxides using Ewald summation implemented *via* VESTA[61] software (see Table S10). However, to improve reliability, the literature-reported Madelung constants of 1.748, 2.400, 2.408 and 4.172 for MnO, Mn_2O_3, MnO_2 and Mn_3O_4, respectively, were utilised.[74] Fig. 4 shows the Bader charge determined using for DFT (U = 0 eV) and DFT+U (U = 2.5 eV) as a function of the formal oxidation state that has been modified with Madelung constant for periodic systems. The Bader charge as a function of the modified formal oxidation state now falls on a single curve, which is best described using a hyperbolic function (see Fig. 4 for the RPBE functional and Fig. S8 for the BEEF-vdW XC functional) with a limit value of 1.8*e* independent of the XC functional used.

The limit-value for the Bader charge on manganese was determined to be 1.8*e*. The presence of a limit value can be ascribed to a "charge self-regulation" effect.[75] Valence electrons around manganese are involved in bonding and anti-bonding orbitals with the surrounding oxygen anions. The bonding state will shift upon changing the formal oxidation state of manganese with the bonding state shifting towards the manganese cation upon increasing the oxidation state, thus compensating for the change in the formal charge.[75,76] Furthermore, to reveal if this trend was unique to Mn bonded to O(H), the relationship between the bonded anion was investigated by substituting the O with S and Se, here it was found that this trend is prominent for oxygen which may be owing to its strong electronegative character in comparison to S and Se (see Fig. S10).

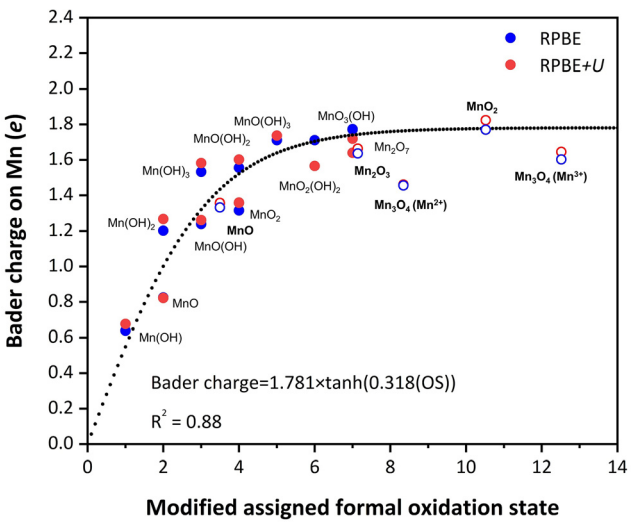

Fig. 4 Bader charge as a function the formal oxidation state modified by Madelung constant of bulk manganese oxides (open symbols: bulk manganese oxides; solid symbols: $Mn_xO_yH_z$ clusters; OS: oxidation state; dotted curve: best fit tanh-function).

$Mn_xO_yH_z$ clusters on fcc-Co(111)

The magnetic moment and Bader charges on Mn on $Mn_xO_yH_z$-Co(111) were evaluated to assess the applicability of the calculated charge correlations on catalyst surfaces. Fig. 5 displays the chosen $Mn_xO_yH_z$ clusters which varied in both ligand complexity and assigned formal oxidation states ranging from +2 to +6. The clusters varied from linear to more complex 3D shapes. For instance, the $Mn_{32}O_{32}$ had a cube-like appearance whilst the $Mn_5O_{13}H_4$ and $Mn_{14}O_{29}H_{12}$ were pyramidal in nature. The calculated magnetic moment on Mn for all the $Mn_xO_yH_z$-Co(111) clusters is $\approx 4.5\mu_B$ (see Table 5) which correlates with a Mn oxidation state of +2. Despite considering clusters with very different formal oxidation states, the magnetic moment remains fairly constant. This suggests that the charge redistribution is largely delocalised as the changes in assigned formal oxidation state did not correspond to changes of the population of the Mn 3d orbital, from which the calculated atomic magnetic moment is predominately derived. Whilst, the calculated Bader charges did show some variation in their values, as it was seen that they also mainly correlate with oxidation states of +2 and +3.

Interestingly, we note that both approaches predict that the cluster stoichiometry is mostly disconnected from the Mn oxidation state: in particular, oxidation states $\leq$+3 are always predicted even when, just based on cluster composition, we would expect oxidation states $\geq$+4. This suggests the existence of a charge transfer from the Co surface that prevents further oxidation of Mn (see Fig. 6).

The marked tendency of Mn to maintain the divalent state, especially predicted by the magnetic moment correlation, can be tentatively ascribed to the particularly stable electronic configuration of Mn^{2+}, namely $[Ar]3d^5$, where the maximum exchange between pairs of parallel-spin electrons significantly reduces the coulombic potential energy. This is in line with several experimental studies predominantly reporting Mn in the +2 state when added as a promoter in Co Fischer–Tropsch catalysts.[77–79] Thus, we argue that the metal surface, acting as an electron reservoir, donates charge to the adsorbed clusters to alleviate the increase in Mn oxidation state, which causes the formal oxidation state to significantly deviate from the cluster

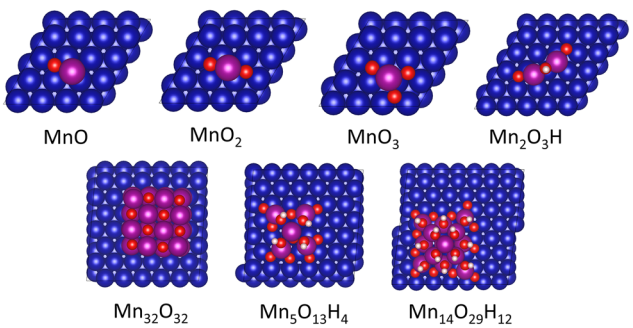

Fig. 5 $Mn_xO_yH_z$ clusters on Co(111), ranging in order of complexity and size, with formal oxidation states ranging from +2 to +6, visualised using VESTA[61] (Mn: purple, Co: blue; O: red; H: white).

Table 5 Calculated Bader charge and magnetic moment on Mn for the $Mn_xO_yH_z$ clusters on a Co(111) surface

$Mn_xO_yH_z$-Co(111)	Assigned formal oxidation state on Mn	Average magnetic moment on Mn[a] (μ_B)/predicted oxidation state	Bader charge on Mn[a] (e)/predicted oxidation state
MnO	+2	4.5/+2	+0.766/+1
MnO_2	+4	4.2/+2	+1.053/+2
Mn_2O_3H	+5	4.4/+2	+1.103/+2
MnO_3	+6	4.4/+2	+1.239/+3
$Mn_{32}O_{32}$	+2	4.5/+2	+1.282/+3
$Mn_5O_{13}H_4$	+4/+5	4.6/+2	+1.396/+3
$Mn_{14}O_{29}H_{12}$	+3/+4	4.6/+2	+1.432/+3

[a] Magnetic moments are reported as absolute values.

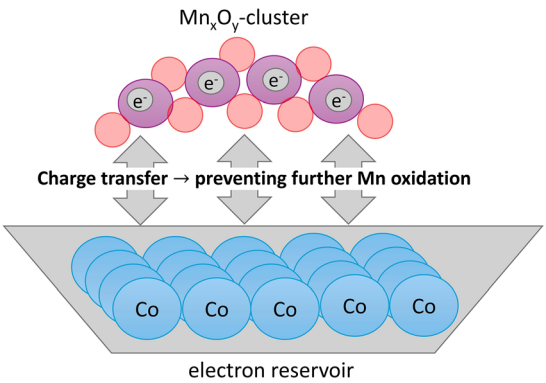

Fig. 6 Schematic representation of charge transfer from cobalt surface (acting as an electron reservoir) to the Mn_xO_y-cluster, this donation of charge suppresses the increase of Mn oxidation state (Mn: purple, Co: blue; O: red).

stoichiometry. This underscores the importance of the correlations derived here, that serve as a powerful tool to reconcile experimentally measured Mn oxidation states with calculated theoretical models.

Conclusions

In conclusion, we have outlined the relationships between the formal oxidation state and calculated magnetic moments and Bader charges of Mn in several bulk and cluster structures, as well as manganese oxide clusters on the Co(111) surface. We found a strong quadratic correlation between Mn magnetic moments and formal oxidation states, that was shown to hold both for Mn oxides bulk and cluster structures. On the other hand, the relationship between the Bader charge and formal oxidation state could be fit with a hyperbolic curve, but only upon modification of the formal oxidation state by the Madelung constant to prevent underestimation of the total coulombic interactions within the bulk manganese oxides. We found that the predicted Bader charges on Mn were largely independent on the Hubbard correction, as similar oxidation state *vs.* Bader charge correlations were obtained with DFT and DFT+U. However, the Hubbard correction had a larger impact on the magnetic properties, as the Mn atomic magnetic moments were higher and closer to experimental values with DFT+U.

The obtained correlations were then applied to estimate the oxidation state of several $Mn_xO_yH_z$ clusters adsorbed on fcc-Co(111). While the predicted Mn oxidation states derived from the magnetic moments were found to be always roughly +2, those calculated according to the Bader charges mildly changed depending on the cluster stoichiometry with values mostly between +2 and +3. Both correlations yielded similar values and revealed that the Mn oxidation states in the $Mn_xO_yH_z$ clusters on the fcc-Co(111) do not align with their cluster stoichiometry. Different results for the oxidation state may be obtained depending on the measurement tool. The atomic magnetic moments correlation was found to be more consistent across different compounds (both bulk and gas-phase molecules) and may be a better indicator for the charge. This may be owing to the spin density being localised at the metal for 3d transition metals,[80] and thus the subtraction of spin-up and spin-down electrons is less prone to error associated with introduced by the boundary of the electron density belonging to an atom. Overall, this work established a method to predict the equivalent formal oxidation state of clusters of manganese oxides adsorbed on metal surfaces. Importantly, this method can enhance the synergy between experiments and theoretical calculations, ultimately facilitating mechanistic understanding and catalyst design. Lastly, the connection between experimental and theoretical data established here can become particularly relevant in light of the recent advances in machine learning interatomic potentials, which enable a substantial computational speed-up hence fast-tracking the surveying of multiple configurations of various chemical compounds[81] that need to be compared against experimental data.

Author contributions

Julie-Ann Hoffman: conceptualization, data curation, formal analysis, investigation, methodology, validation, visualization, writing – original draft, writing – review & editing. Enrico Sireci: conceptualization, data curation, formal analysis, investigation, methodology, validation, writing – original draft, writing – review & editing. Thobani Gambu: conceptualization, data curation, supervision, writing – review & editing. Dmitry I. Sharapa: conceptualization, data curation, supervision, writing – review & editing. Felix Studt: conceptualization, funding acquisition, methodology, project administration, resources, supervision, writing – review & editing. Eric van

Steen: conceptualization, funding acquisition, methodology, project administration, resources, supervision, writing – review & editing.

Conflicts of interest

There are no conflicts to declare.

Data availability

Additional data has been made available in the supplementary information (SI). Supplementary information: phonon calculation data with regards to ZPE, $\Delta H^{0\rightarrow 298K}$ and S^{0}_{vib} of Mn oxides studied and related experimental data sourced from literature. All information regarding the U_{eff} calculation. The magnetic and geometric data for both RPBE and BEEF-vdW for both DFT and DFT+U methods. The magnetic ordering for the bulk Mn oxides and magnetic moment data for all structures studied. All data related to the BEEF-vdW for magnetic moment and Bader charges compared to formal assigned formal oxidation state on Mn. See DOI: https://doi.org/10.1039/d6cp00917d.

Structural files will be supplied upon request and uploaded on to a free server (ZivaHub) in due course.

Acknowledgements

We gratefully acknowledge that this study is supported by the German Federal Ministry of Research, Technology and Space (BMFTR) within the CARE-O-SENE project (03SF0673). The authors thank the Council for Scientific and Industrial Research's (CSIR's) Centre for High Performance Computing (CHPC), the University of Cape Town's ICTS High Performance Computing team, https://hpc.uct.ac.za/. The authors acknowledge support by the state of Baden-Württemberg through bwHPC and the German Research Foundation (DFG) through grant no. INST 40/575-1 FUGG (JUSTUS 2 cluster, RVs bw17D011). We gratefully acknowledge the financial support of the National Research Foundation (NRF) and DSI-NRF SARChI (UID: 114606). Support from the Helmholtz Association is also gratefully acknowledged.

Notes and references

1 A. Walsh, A. A. Sokol, J. Buckeridge, D. O. Scanlon and C. R. A. Catlow, *Nat. Mater.*, 2018, **17**, 958–964.
2 S. A. Chambers, P. V. Sushko and P. S. Bagus, *J. Vac. Sci. Technol., A*, 2025, **43**, 023203.
3 F. Yang, J. Graciani, J. Evans, P. Liu, J. Hrbek, J. Fdez. Sanz and J. A. Rodriguez, *J. Am. Chem. Soc.*, 2011, **133**, 3444–3451.
4 D. F. Leto and T. A. Jackson, *Inorg. Chem.*, 2014, **53**, 6179–6194.
5 K. Ray, T. Petrenko, K. Wieghardt and F. Neese, *Dalton Trans.*, 2007, 1552.
6 K. Ray, T. Weyhermüller, F. Neese and K. Wieghardt, *Inorg. Chem.*, 2005, **44**, 5345–5360.
7 M. Wang, J. England, T. Weyhermüller, S.-L. Kokatam, C. J. Pollock, S. DeBeer, J. Shen, G. P. A. Yap, K. H. Theopold and K. Wieghardt, *Inorg. Chem.*, 2013, **52**, 4472–4487.
8 M. A. Spackman, *Chem. Rev.*, 1992, **92**, 1769–1797.
9 N. K. Hansen and P. Coppens, *Acta Crystallogr. Sect. A*, 1978, **34**, 909–921.
10 T. S. Koritsanszky and P. Coppens, *Chem. Rev.*, 2001, **101**, 1583–1628.
11 S. C. Bart, K. Chłopek, E. Bill, M. W. Bouwkamp, E. Lobkovsky, F. Neese, K. Wieghardt and P. J. Chirik, *J. Am. Chem. Soc.*, 2006, **128**, 13901–13912.
12 T. Petrenko, K. Ray, K. E. Wieghardt and F. Neese, *J. Am. Chem. Soc.*, 2006, **128**, 4422–4436.
13 R. G. Serres, C. A. Grapperhaus, E. Bothe, E. Bill, T. Weyhermüller, F. Neese and K. Wieghardt, *J. Am. Chem. Soc.*, 2004, **126**, 5138–5153.
14 P. Surawatanawong, S. Sproules, F. Neese and K. Wieghardt, *Inorg. Chem.*, 2011, **50**, 12064–12074.
15 C. F. Matta and R. J. Gillespie, *J. Chem. Educ.*, 2002, **79**, 1141.
16 M. Xie, X. Zhang, R. Wang, Y. Jiao, Z. Shu, S. Shan, Y. Bian, H. Lin, J. Chen and Y. Xu, *Chem. Eng. J.*, 2024, **494**, 152908.
17 K. Wang, H. Zhuo, J. Wang, F. Poon, X. Sun and B. Xiao, *Adv. Funct. Mater.*, 2023, **33**, 2212607.
18 X. Zhang, S. Liu, B. Wang, G. Wang, H. Du, X. Wang, H. Zhang, S. Zhao, L. Wang and H. Yu, *Sci. China: Chem.*, 2024, **67**, 87–105.
19 M. R. A. Kishore, H. Okamoto, L. Patra, R. Vidya, A. O. Sjåstad, H. Fjellvåg and P. Ravindran, *Phys. Chem. Chem. Phys.*, 2016, **18**, 27885–27896.
20 K. Alshehri, *Appl. Phys. A: Mater. Sci. Process.*, 2025, **131**, 55.
21 H. Waqas, A. H. Qureshi and M. Shahzad, *Acta Metall. Sin. Engl. Lett.*, 2015, **28**, 159–163.
22 M. M. N. Ansari, S. Khan and N. Ahmad, *J. Alloys Compd.*, 2020, **831**, 154778.
23 V. Vermaak, R. D. Cunningham, J. H. Potgieter, J. M. Botha, E. van Steen, M. Claeys, M. Fadlalla, J.-A. Hoffman, S. Abdullah, E. Sireci, F. Studt, A. Zimina, J.-D. Grunwaldt, C. Hsu, M. Wolf, C. E. Jimenez, P. Sakoglu and D. J. Moodley, *Catal. Sci. Technol.*, 2026, **16**, 1488–1530.
24 E. Ø. Pedersen, I.-H. Svenum and E. A. Blekkan, *J. Catal.*, 2018, **361**, 23–32.
25 S. S. Gupta, P. M. Shenai, J. Meeuwissen, G. L. Bezemer and S. Shetty, *J. Phys. Chem. C*, 2021, **125**, 21390–21401.
26 M. Zhang, S. Chi, H. Huang and Y. Yu, *Appl. Surf. Sci.*, 2021, **567**, 150854.
27 C. L. Tucker, Y. Ragoo, S. Mathe, L. Macheli, A. Bordoloi, T. C. R. Rocha, S. Govender, P. J. Kooyman and E. Van Steen, *J. Catal.*, 2022, **411**, 97–108.
28 M. Gençoğlu, Masters dissertation, İzmir Institute of Technology, Izmir, Turkey, 2019.
29 M. V. Doorslaer, Masters dissertation, Ghent University, Ghent, Belgium, 2017.
30 K. Krupski, M. Moors, P. Jóźwik, T. Kobiela and A. Krupski, *Materials*, 2015, **8**, 2935–2952.
31 T. Diemant, K. M. Schüttler and R. J. Behm, *Chem. Phys. Chem.*, 2015, **16**, 2943–2952.

32 H. Li, X. Weng, Z. Tang, H. Zhang, D. Ding, M. Chen and H. Wan, *ACS Catal.*, 2018, **8**, 10156–10163.
33 H. Chen, Y. Liu, F. Yang, M. Wei, X. Zhao, Y. Ning, Q. Liu, Y. Zhang, Q. Fu and X. Bao, *J. Phys. Chem. C*, 2017, **121**, 10398–10405.
34 G. Pacchioni, *Phys. Chem. Chem. Phys.*, 2013, **15**, 1737.
35 I. Choudhuri and D. G. Truhlar, *J. Chem. Theory Comput.*, 2020, **16**, 5884–5892.
36 W. Tang, E. Sanville and G. Henkelman, *J. Phys.: Condens. Matter*, 2009, **21**, 084204.
37 E. Sanville, S. D. Kenny, R. Smith and G. Henkelman, *J. Comput. Chem.*, 2007, **28**, 899–908.
38 G. Henkelman, A. Arnaldsson and H. Jónsson, *Comput. Mater. Sci.*, 2006, **36**, 354–360.
39 J. Reed and G. Ceder, *Electrochem. Solid-State Lett.*, 2002, **5**(7), A145–A148.
40 J. Reed and G. Ceder, *Chem. Rev.*, 2004, **104**, 4513–4534.
41 B. Deng, P. Zhong, K. Jun, J. Riebesell, K. Han, C. J. Bartel and G. Ceder, *Nat. Mach. Intell.*, 2023, **5**, 1031–1041.
42 L. Barroso-Luque, P. Zhong, J. H. Yang, F. Xie, T. Chen, B. Ouyang and G. Ceder, *Phys. Rev. B*, 2022, **106**, 144202.
43 G. Kresse and J. Hafner, *Phys. Rev. B*, 1993, **47**, 558–561.
44 G. Kresse and J. Furthmüller, *Phys. Rev. B*, 1996, **54**, 11169–11186.
45 B. Hammer, L. B. Hansen and J. K. Nørskov, *Phys. Rev. B*, 1999, **59**, 7413–7421.
46 J. Wellendorff, K. T. Lundgaard, A. Møgelhøj, V. Petzold, D. D. Landis, J. K. Nørskov, T. Bligaard and K. W. Jacobsen, *Phys. Rev. B*, 2012, **85**, 235149.
47 G. Kresse and D. Joubert, *Phys. Rev. B*, 1999, **59**, 1758–1775.
48 P. E. Blöchl, *Phys. Rev. B*, 1994, **50**, 17953–17979.
49 H. J. Monkhorst and J. D. Pack, *Phys. Rev. B*, 1976, **13**, 5188–5192.
50 M. Yu and D. R. Trinkle, *J. Chem. Phys.*, 2011, **134**, 064111.
51 A. J. Cohen, P. Mori-Sánchez and W. Yang, *Science*, 2008, **321**, 792–794.
52 S. L. Dudarev, G. A. Botton, S. Y. Savrasov, C. J. Humphreys and A. P. Sutton, *Phys. Rev. B*, 1998, **57**, 1505–1509.
53 C. Loschen, J. Carrasco, K. M. Neyman and F. Illas, *Phys. Rev. B*, 2007, **75**, 035115.
54 M. Capdevila-Cortada, Z. Łodziana and N. López, *ACS Catal.*, 2016, **6**, 8370–8379.
55 R. O. Jones and O. Gunnarsson, *Rev. Mod. Phys.*, 1989, **61**, 689–746.
56 D. C. Patton, D. V. Porezag and M. R. Pederson, *Phys. Rev. B*, 1997, **55**, 7454–7459.
57 M. Posternak, A. Baldereschi, S. Massidda and N. Marzari, *Phys. Rev. B*, 2002, **65**, 184422.
58 M. Regulski, R. Przeniosło, I. Sosnowska, D. Hohlwein and R. Schneider, *J. Alloys Compd.*, 2004, **362**, 236–240.
59 B. Boucher, R. Buhl and M. Perrin, *J. Appl. Phys.*, 1971, **42**, 1615–1617.
60 Y. Noda, K. Ohno and S. Nakamura, *Phys. Chem. Chem. Phys.*, 2016, **18**, 13294–13303.
61 K. Momma and F. Izumi, *J. Appl. Crystallogr.*, 2011, **44**, 1272–1276.
62 S. Geller and G. P. Espinosa, *Phys. Rev. B*, 1970, **1**, 3763–3769.
63 M. C. Kemei, J. K. Harada, R. Seshadri and M. R. Suchomel, *Phys. Rev. B*, 2014, **90**, 064418.
64 A. A. Bolzan, C. Fong, B. J. Kennedy and C. J. Howard, *Aust. J. Chem.*, 1993, **46**(6), 939–944.
65 M. Guo, Y.-M. Lee, R. Gupta, M. S. Seo, T. Ohta, H.-H. Wang, H.-Y. Liu, S. N. Dhuri, R. Sarangi, S. Fukuzumi and W. Nam, *J. Am. Chem. Soc.*, 2017, **139**, 15858–15867.
66 G. V. Gibbs, R. T. Downs, D. F. Cox, K. M. Rosso, N. L. Ross, A. Kirfel, T. Lippmann, W. Morgenroth and T. D. Crawford, *J. Phys. Chem. A*, 2008, **112**, 8811–8823.
67 S. F. Saipuddin, M. F. M. Taib, A. Hashim, N. E. Suhaimi and S. A. Senawi, *Mater. Today Proc.*, 2023, S2214785323020862.
68 X. G. Zhao, W. H. Richardson, J.-L. Chen, J. Li, L. Noodleman, H.-L. Tsai and D. N. Hendrickson, *Inorg. Chem.*, 1997, **36**, 1198–1217.
69 M. Schüler, O. E. Peil, G. J. Kraberger, R. Pordzik, M. Marsman, G. Kresse, T. O. Wehling and M. Aichhorn, *J. Phys.: Condens. Matter*, 2018, **30**, 475901.
70 T. A. Manz and N. G. Limas, *RSC Adv.*, 2016, **6**, 47771–47801.
71 N. G. Limas and T. A. Manz, *RSC Adv.*, 2018, **8**, 2678–2707.
72 D. Tabor, *Gases, Liquids and Solids: And Other States of Matter*, Cambridge University Press, 3rd edn, 1991.
73 D. Argyriou and C. Howard, *Aust. J. Phys*, 1992, **45**, 239.
74 W. D. Haynes, *Handbook of Chemistry and Physics*, CRC Press, 95th edn, 2014.
75 H. Raebiger, S. Lany and A. Zunger, *Nature*, 2008, **453**, 763–766.
76 X. Guo, E. Song, W. Zhao, S. Xu, W. Zhao, Y. Lei, Y. Fang, J. Liu and F. Huang, *Nat. Commun.*, 2022, **13**, 5954.
77 G. R. Johnson, S. Werner and A. T. Bell, *ACS Catal.*, 2015, **5**, 5888–5903.
78 T. F. Kimpel, J.-X. Liu, W. Chen, R. Pestman and E. J. M. Hensen, *J. Catal.*, 2023, **425**, 181–195.
79 F. Morales, E. Desmit, F. Degroot, T. Visser and B. Weckhuysen, *J. Catal.*, 2007, **246**, 91–99.
80 M. P. Johansson, M. R. A. Blomberg, D. Sundholm and M. Wikström, *Biochim. Biophys. Acta, Bioenerg.*, 2002, **1553**, 183–187.
81 K. Chen, Y. Wu, H. Li, L. Ma, J. Ye, X. Zhang, J. Rong, X. Yu and Y. Yang, *J. Mater. Chem. A*, 2026, **14**, 8380–8392.